Asian Journal of Chemistry; Vol. 38, No. 3 (2026), 589-600
ASIAN JOURNAL OF CHEMISTRY
https://doi.org/10.14233/ajchem.2026.35026

Synthesis of Pure and Ag-doped $CuFe_2O_4$ Nanoparticles using a Microwave-Assisted Biosynthesis Method and Investigation of their Antioxidant and Antimicrobial Activity

SUNIL P. GAWALI[1,2,*], P.B. ABHANGE[3], RAM S. BARKULE[4], A.V. RAUT[5] and D.V. MANE[2,6]

[1]Department of Chemistry, Sundarrao More Arts, Commerce and Science College, Poladpur, Raigad-402303, India
[2]School of Science, Yashwantrao Chavan Maharashtra Open University, Nashik-402222, India
[3]Department of Physics, G.M. Vedak College of Science, Tala Raigad-402111, India
[4]Department of Physics, Sundarrao More Arts, Commerce and Science College, Poladpur, Raigad-402303, India
[5]Department of Physics, Vivekanand Arts, Sardar Dalip Singh Commerce and Science College, Aurangabad-431001, India
[6]Department of Chemistry, Shri Chhatrapati Shivaji College Omerga, Dharashiv-413606, India

*Corresponding author: E-mail: spgawali1986@gmail.com

Received: 7 October 2025 *Accepted*: 18 December 2025 *Published online*: 6 March 2026 AJC-22277

This study reports the successful synthesis and characterisation of silver-doped copper ferrites nanoparticles ($Ag_xCu_{1-x}Fe_2O_4$, where x = 0.05, 0.1, 0.2) through microwave-assisted biosynthesis employing *Asteracantha longifolia* leaf extract as a reducing and stabilizing agent. X-ray diffraction analysis (XRD) confirmed the formation of single-phase cubic spinel structures with systematic lattice parameter variations from 8.294 to 8.165 Å upon silver incorporation. Electron microscopy (SEM) revealed morphological evolution from spherical to irregular geometries with crystallite sizes ranging between 15.43-18.85 nm. The substitutional mechanism of Ag^+ ions into tetrahedral and octahedral sites was evidenced by structural refinement, demonstrating successful dopant integration without phase segregation. Spectroscopic investigations revealed enhanced optical absorption in the UV-visible region (300-800 nm) due to surface plasmon resonance effects of silver nanodomains. Magnetic characterisation showed decreased saturation magnetisation values correlating with silver content, attributed to the diamagnetic nature of Ag^+ ions disrupting magnetic exchange interactions. Thermal gravimetric analysis indicated structural stability up to 600 ºC with minimal mass loss. Antioxidant evaluation through DPPH radical scavenging demonstrated concentration-dependent activity enhancement, with $Ag_{0.2}Cu_{0.8}Fe_2O_4$ exhibiting 55.35% radical neutralisation efficiency compared to 41.87% for undoped copper ferrite. The improved performance stems from increased electron-donating capacity facilitated by the electronic properties of silver, establishing these nanocomposites as promising materials for advanced oxidative stress mitigation applications in biomedical and environmental sectors.

Keywords: *Asteracantha longifolia*, Microwave assisted sol-gel synthesis, Ferrites, Antimicrobial activity.

INTRODUCTION

Spinel ferrite nanoparticles (NPs), especially those with a copper ferrite ($CuFe_2O_4$) composition, are a class of nanocrystalline materials garnering significant scientific attention. Their unique combination of magnetic, electrical and catalytic properties, along with high thermal stability and chemical inertness, makes them ideal for a broad spectrum of applications, including magnetic data storage, catalysis, ferrofluids, biosensors and environmental remediation [1,2]. Copper ferrite ($CuFe_2O_4$) nanostructures exhibit exceptional magnetoelectrical characteristics coupled with robust catalytic functionality, demonstrating remarkable thermodynamic stability and chemical resistance under extreme operational conditions. Modern synthetic techniques for spinel-type compounds include co-precipitation methods, solvothermal crystallization, lyophilization, microemulsion templating and sol-gel polymerization [3]. The sol-gel auto-combustion strategy represents a particularly efficacious route for generating monodisperse nanocrystalline particles under moderate thermal conditions [4,5]. Microwave assisted sol-gel auto-combustion method using citric acid as fuel in *Asteracantha longifolia* leave extract provides a sustainable synthesis route. This approach reduces reliance on costly reagents and toxic precursors while lowering energy consumption through rapid microwave heating, making it a more eco-friendly method for material synthesis.

A. longifolia, a medicinally significant species in traditional Ayurvedic pharmacopeia [6], contains abundant bioactive metabolites including fatty acid esters [7], polyphenolic antioxidants [7], mineral cofactors [8], proanthocyanidin oligomers [9], nitrogenous alkaloids [10], enzymatic proteins [11], amino acid residues [12], terpenoid compounds [13], vitamin complexes [14] and glycosidic derivatives [15]. These constituents confer therapeutic properties against hematological disorders, nephropathies, diabetic complications, oncological conditions and exhibit antifungal, cytotoxic, anti-inflammatory, antipyretic, antioxidant, insecticidal, immunomodulatory, hepatoprotective, antiplatelet and antiviral activities [6-21]. Pioneer investigations by Dubey *et al.* [22] demonstrated the inaugural microwave assisted sol-gel-auto combustion approach for metallic nanoparticle fabrication using *Hygrophila spinosa* aqueous extracts to produce auriferous nanostructures. Subsequently, Mohamed *et al.* [23] explored argentiferous nanoparticle biosynthesis, while Nayak *et al.* [24] employed hydroethanolic *H. auriculata* extracts for silver nanoparticle generation. Uma *et al.* [25] successfully synthesised silver-incorporated copper ferrite nanocomposites exhibiting dual spinel crystallographic phases *via* jatropha oil-mediated combustion methodology.

This investigation addresses the microwave-assisted sol-gel synthetic production of pristine and silver-modified copper ferrite nanomaterials utilizing *A. longifolia* foliar extracts as reducing and capping agents. The primary objective encompasses the controlled fabrication of Ag-$CuFe_2O_4$ and $CuFe_2O_4$ nanoparticles possessing distinctive microstructural architectures and enhanced physico-chemical properties [26-28].

EXPERIMENTAL

Preparation of *Asteracantha longifolia* extract: Fresh *A. longifolia* (*H. auriculata*) leaves were collected from the Mahad city, district Raigad (18.083ºN, 73.417ºE) as shown in Fig. 1. The leaves were washed thoroughly with tap water to remove surface impurities and were subsequently rinsed using double-distilled water. The cleaned leaves were then shade-dried for a period of four days. After drying, the material was pulverized into a fine powder using a mortar and pestle and stored in an airtight container for further use. About 20 g of powder plant material was taken into a 500 mL flask consisting of 200 mL of water and heated it for 3 min in microwave at 350 W following the 30 min in ultrasound. The water extract of *A. longifolia* was then collected into a beaker by using a Whatman's no. 41 filter paper and the filtrate was store in the refrigerator for further experiments.

Biosynthesis of copper ferrite ($CuFe_2O_4$) NPs: The $CuFe_2O_4$ nanoparticles were synthesized by a microwave-assisted sol-gel auto-combustion method using citric acid as a fuel in the presence of *A. longifolia* leaf extract. Briefly, $Cu(NO_3)_2{\cdot}3H_2O$, $Fe(NO_3)_3{\cdot}9H_2O$ and citric acid were separately dissolved in 50 mL of deionized water, maintaining a metal salt to citric acid molar ratio of 1:3. Subsequently, 20 mL of the plant extract was added to the solution followed by the addition of ammonium hydroxide dropwise to adjust the pH to 7. The resulting mixture was heated and magnetically stirred in a microwave oven at 80 ºC until gel formation occurred. The obtained gel was further heated at 140 ºC for a short duration in the microwave, which led to spontaneous auto-combustion and the formation of ferrite powder. The as-pre-

(a) Fresh *A. longifolia* plant showing characteristic purple flowers and spiny stems in its natural habitat

(b) Dried and processed *A. longifolia* leaves prepared for aqueous extraction. Images were captured in Cholai, Maharashtra, India (GPS coordinates: 17º9'12" N, 73º46'8" E)

Fig. 1. Images of *Asteracantha longifolia* plant material

pared powder was calcined in a muffle furnace at 700 ºC for 3 h.

Biosynthesis of silver-doped copper NPs: The Ag-doped $CuFe_2O_4$ NPs were prepared using the same method that was followed in biosynthesis of copper ferrite ($CuFe_2O_4$) NPs, in varying concentrations. Briefly, three silver doped-$CuFe_2O_4$ nanoparticles (5%Ag-$CuFe_2O_4$, 10%Ag-$CuFe_2O_4$ and 20%Ag-$CuFe_2O_4$) were synthesised by adding cupric nitrate, ferric nitrate and silver nitrate $AgNO_3$ in the ratio of $Ag_xCu_{1-x}Fe_2O_4$ (x = 0.05, 0.1, 0.2).

Antibacterial assays

Disk diffusion method: Antibiotic susceptibility assays for the $CuFe_2O_4$ and all Ag-doped $CuFe_2O_4$ nanocomposites were tested against the Gram-positive bacterium *Bacillus subtilis*, *Staphylococcus aureus* and Gram-negative bacterium *Salmonella typhimurium* and *Klebsiella pneumonia* using disk diffusion method on Mueller-Hinton agar plates [29]. The 100 mg $CuFe_2O_4$ and $CuFe_2O_4$ nanoparticles sonicated in distilled water were pipetted on to individual inoculated agar plates and then incubated at 37 ºC for 24 h before that the microorganisms were cultured into nutrient broth medium and incubated at 37 ºC for 6 h. Each strain was swabbed uniformly on to agar plates [30] and 6 mm diameter disc were placed in agar plate and on which 20 µL (1 mg/mL) nanoparticles were loaded. The standard antibiotic streptomycin [31] was also loaded as control to monitor any contamination during testing. Zones of inhibition surrounding the coated samples were measured by ruler scale as a parameter of antibacterial property of the synthesised $CuFe_2O_4$ and Ag doped $CuFe_2O_4$ [32,33].

Evaluation of DPPH free radical scavenging activity: The antioxidant activity of $CuFe_2O_4$ and Ag doped $CuFe_2O_4$ nanoparticles was evaluated by means of 2,2-diphenyl-1-picrylhydrazyl hydrate (DPPH) free radical scavenging assay by with slightly modification. In brief, different concentrations of $CuFe_2O_4$ or Ag doped Fe_2O_4 nanoparticles (25, 50, 75, 100 and 150 µg/mL) were added to 50 mL of 0.1 mM DPPH solution and placed under dark condition at room temperature for 30 min to facilitate the reaction. After that, the absorbance of solution was recorded at 517 nm wavelengths by using ethanol as blank solvent. The inhibition parentage of free radicals was calculated based on the formula as follows [34-36]:

$$\text{DPPH scavenging activity (\%)} = \frac{A_c - A_s}{A_c} \times 100$$

where A_c = O.D. of control (standard) and A_s = O.D. of sample.

RESULTS AND DISCUSSION

Thermal studies: The thermogram of biosynthesised $Ag_xCu_{1-x}Fe_2O_4$ (x = 0.05, 0.1, 0.2) nanoparticles reveals a multi-stage thermal decomposition process with excellent thermal stability as shown in Fig. 2. The material exhibits minimal weight loss (0.864%) up to approximately 100 ºC, likely attributed to the desorption of physisorbed water and volatile impurities. A more significant decomposition stage occurs between 100-300 ºC with a 5.210% weight loss, corresponding to the removal of chemisorbed water, organic residues from synthesis and possible structural hydroxyl groups. The major thermal event happens between 300-600 ºC with a substantial 24.144% weight loss, which can be attributed to the decomposition of organic ligands, carbonaceous materials or precursor residues and potentially some structural rearrangement of the spinel ferrite matrix. Beyond 600 ºC, the material demonstrates remarkable thermal stability with only minor weight changes, indicating the formation of a stable Ag-doped $CuFe_2O_4$ crystalline phase. The final residue of 69.782% suggests the successful incorporation of silver dopant into the copper ferrite structure, with the silver doping likely enhancing the thermal stability of the spinel framework and potentially improving the magnetic and catalytic properties of material for high-temperature applications [37,38].

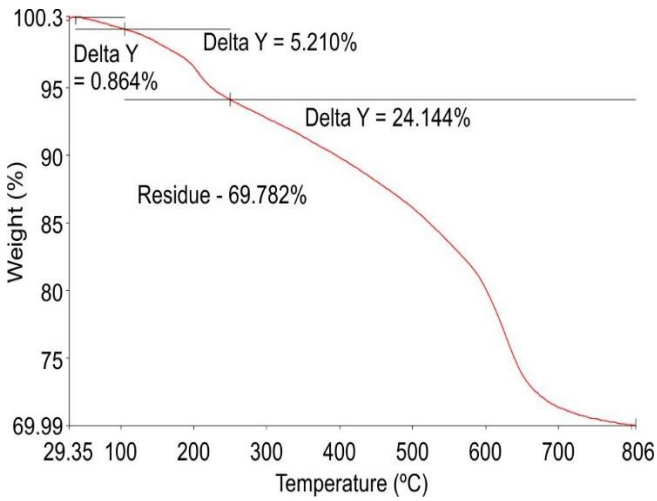

Fig. 2. Thermogram of microwave assisted synthesized Ag-doped $CuFe_2O_4$ nanocomposites

X-ray diffraction studies: The X-ray diffraction patterns of Ag-doped $CuFe_2O_4$ nanoparticles demonstrate the successful formation of the cubic spinel structure with systematic changes upon silver incorporation. All samples exhibit characteristic diffraction peaks at 2θ values of approximately 18.3º, 30.1º, 35.5º, 43.1º, 53.4º, 57.0º and 62.6º, corresponding to the (111), (220), (311), (400), (422), (511) and (440) crystallographic planes of the cubic spinel ferrite structure, respectively (Fig. 3). The most intense peak at 35.5º corresponds to the (311) plane, which is typical for spinel ferrites. As the silver doping concentration increases from 5% to 20%, there is a notable enhancement in peak intensity and sharpness, particularly evident in the (311) reflection, indicating improved crystallinity and larger crystallite size with higher Ag content. The absence of additional peaks corresponding to metallic silver or silver oxide phases suggests that silver ions are successfully incorporated into the spinel lattice structure, likely substituting for Cu^{2+} or Fe^{3+} ions. The slight peak broadening observed in lower doping concentrations may be attributed to smaller crystallite sizes and lattice strain effects, while the progressive narrowing with increased silver content indicates reduced lattice distortion and enhanced structural ordering, confirming the stabilizing effect of silver doping on the copper ferrite spinel framework [37,38].

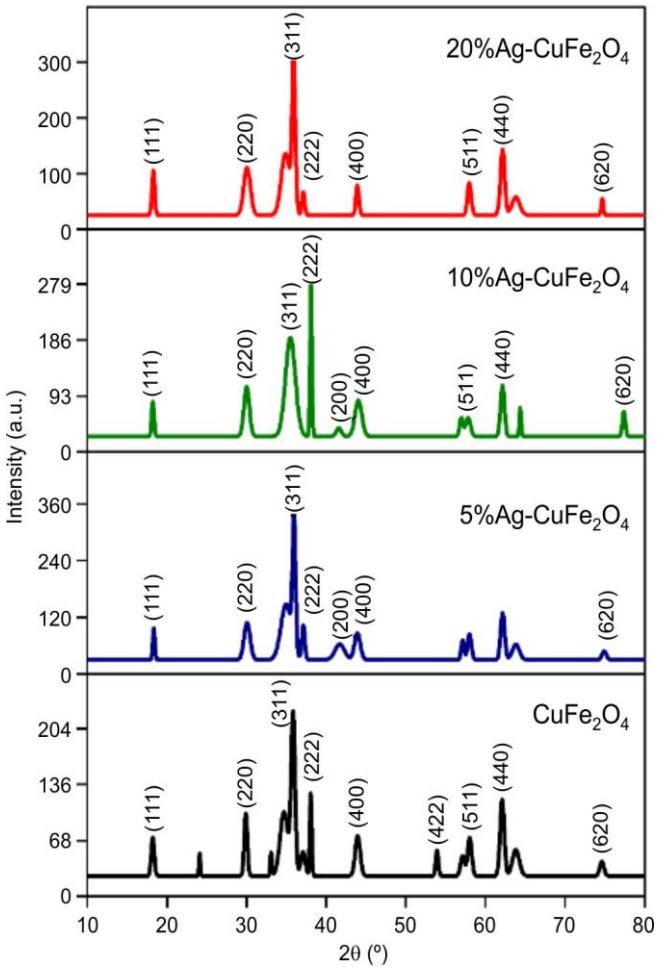

Fig. 3. XRD patterns of microwave assisted synthesized $Ag_xCu_{1-x}Fe_2O_4$ (x = 0.05, 0.1, 0.2) nanocomposites

X-ray diffraction parameters of Ag-doped $CuFe_2O_4$ nanoparticles reveal significant structural and morphological changes with varying silver concentrations. The lattice parameter 'a' shows a non-monotonic trend, decreasing from 8.294 Å for pure $CuFe_2O_4$ to 8.270 Å for 5% Ag-doping, reaching a minimum of 8.165 Å at 10% Ag-doping, before increasing to 8.240 Å at 20% Ag-doping, indicating complex substitution mechanisms and possible phase segregation at higher doping concentrations as shown in Table 1a-d. The crystallite sizes calculated using the Scherrer's equation demonstrate the considerable variation across different compositions, with average values of 15.43 nm, 15.56 nm, 16.49 nm and 18.85 nm for undoped, 5%, 10% and 20% Ag-doped samples, respectively, suggesting that 10% silver doping promotes the optimal crystal growth. The full-width half-maximum (FWHM) values exhibit substantial fluctuations ranging from 0.26º to 1.45º with the 10% Ag-doped sample showing the most pronounced peak broadening for certain reflections, indicating increased lattice strain and structural disorder at this composition. Individual crystallite sizes for specific reflections vary dramatically from 5.76 nm to 36.07 nm, reflecting anisotropic growth patterns and heterogeneous size distributions, while the retention of all cubic spinel reflections across all compositions confirms successful solid solution formation without secondary phase precipitation [39] as shown in Table 2a-d.

FTIR studies: The FTIR spectra of Ag-doped $CuFe_2O_4$ nanoparticles reveal characteristic vibrational modes of the spinel ferrite structure with systematic changes upon silver incorporation. All the samples exhibit the fundamental metal-oxygen stretching vibrations in the fingerprint region, with prominent peaks around 651-579 cm^{-1} and 428-419 cm^{-1} corresponding to the tetrahedral (Fe^{3+}–O) and octahedral (Cu^{2+}/Fe^{3+}–O) site vibrations, respectively, confirming the cubic spinel structure. The broad absorption bands in the 3500-3000 cm^{-1} region and around 1640 cm^{-1} are attributed to O–H stretching and bending vibrations of surface-adsorbed water molecules and hydroxyl groups [40]. Spectral changes occur with increasing silver doping concentration, particularly the appearance of additional peaks around 1129-1125 cm^{-1} and shifts in the metal-oxygen stretching frequencies, suggesting structural modifications and possible changes in bond lengths due to silver doping in the spinel lattice. The peaks around 2287-2269 cm^{-1} and 2946-2940 cm^{-1} may be attributed to the residual organic compounds from the synthesis process or carbonate groups as shown in Fig. 4. The systematic evolution of peak positions and intensities, particularly the metal-oxygen vibrations shifting from 393 cm^{-1} in pure $CuFe_2O_4$ to 428 cm^{-1} in 20% Ag-doped sample, indicates the successful incorporation of Ag^+ into the crystal structure and confirms the formation of Ag-doping copper ferrite with modified local coordination environments [41,42].

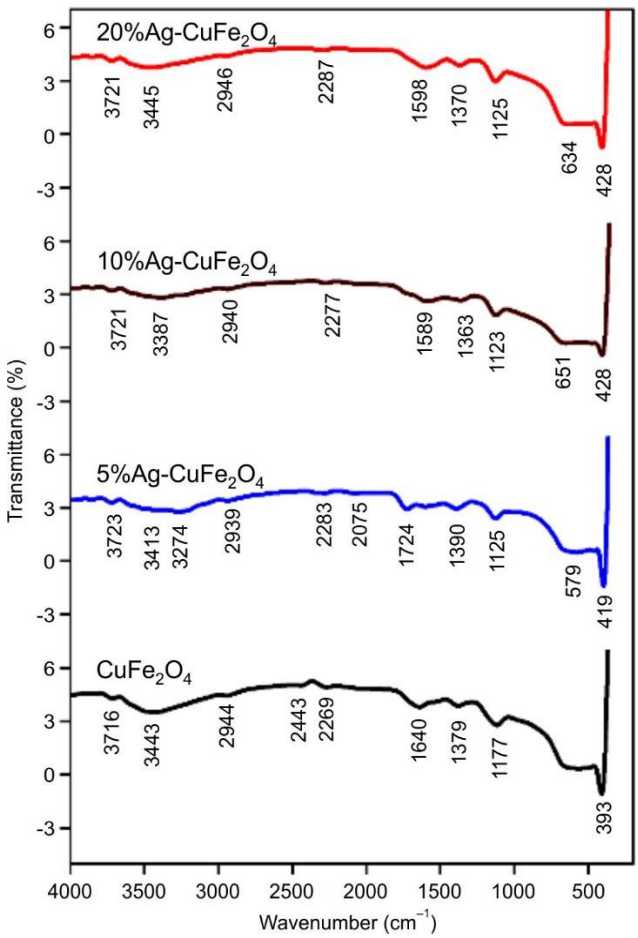

Fig. 4. FTIR spectra of microwave assisted synthesized $Ag_xCu_{(1-x)}Fe_2O_4$ (x = 0.05, 0.1, 0.2) nanocomposites

TABLE-1
CRYSTALLOGRAPHIC PARAMETERS VALUES OF $Ag_xCu_{1-x}Fe_2O_4$ (x = 0.05, 0.1, 0.2) NANOCOMPOSITES

Miller indices			Diffraction angles		Sine values		Interplanar spacing	Lattice parameters	
h	*k*	*l*	2θ	θ	Sin θ	2Sin θ	d	$(a/d)^2$	a
(a) $CuFe_2O_4$									
1	1	1	18.214	9.107	0.158	0.317	4.865	2.966	8.427
2	2	0	29.899	14.949	0.258	0.516	2.985	7.880	8.444
3	1	1	35.839	17.919	0.308	0.615	2.503	11.209	8.301
2	2	2	37.074	18.537	0.318	0.636	2.422	11.968	8.391
4	0	0	43.946	21.973	0.374	0.748	2.058	16.577	8.233
4	2	2	53.926	26.963	0.453	0.907	1.698	24.343	8.321
5	1	1	58.032	29.016	0.485	0.970	1.588	27.859	8.250
4	4	0	63.827	31.914	0.529	1.057	1.457	33.090	8.241
6	2	0	74.623	37.312	0.606	1.212	1.271	43.505	8.035
									8.294
(b) 5%Ag-$CuFe_2O_4$									
1	1	1	18.350	9.175	0.159	0.319	4.830	3.011	8.365
2	2	0	30.059	15.030	0.259	0.519	2.970	7.963	8.400
3	1	1	35.958	17.979	0.309	0.617	2.495	11.282	8.275
2	2	2	37.121	18.560	0.318	0.637	2.419	11.997	8.381
4	0	0	43.913	21.957	0.374	0.748	2.060	16.554	8.239
5	1	1	58.018	29.009	0.485	0.970	1.588	27.846	8.252
4	4	0	63.839	31.920	0.529	1.058	1.457	33.102	8.239
6	2	0	74.929	37.465	0.608	1.217	1.266	43.810	8.007
									8.270
(c) 10%Ag-$CuFe_2O_4$									
1	1	1	18.224	9.112	0.158	0.317	4.863	2.970	8.423
2	2	0	30.010	15.005	0.259	0.518	2.975	7.937	8.413
3	1	1	35.505	17.752	0.305	0.610	2.526	11.008	8.377
2	2	2	38.082	19.041	0.326	0.653	2.361	12.603	8.177
3	2	1	44.041	22.020	0.375	0.750	2.054	16.646	7.685
5	1	1	57.836	28.918	0.484	0.967	1.593	27.688	8.275
4	4	0	64.387	32.194	0.533	1.066	1.445	33.611	8.177
6	2	0	77.393	38.696	0.625	1.251	1.232	46.281	7.791
									8.165
(d) 20%Ag-$CuFe_2O_4$									
1	1	1	18.286	9.143	0.159	0.318	4.846	2.990	8.394
2	2	0	30.057	15.029	0.259	0.519	2.970	7.962	8.400
3	1	1	34.905	17.452	0.300	0.600	2.568	10.651	8.516
2	2	2	37.107	18.554	0.318	0.636	2.420	11.989	8.384
3	2	1	43.919	21.960	0.374	0.748	2.059	16.558	7.705
5	1	1	57.994	28.997	0.485	0.970	1.589	27.825	8.255
4	4	0	63.837	31.919	0.529	1.058	1.457	33.100	8.240
6	2	0	74.689	37.344	0.607	1.213	1.270	43.570	8.029
									8.240

UV-Vis spectral studies: The UV-Vis absorption spectra of Ag-doped $CuFe_2O_4$ nanoparticles (Fig. 5) demonstrate the significant optical property modifications upon silver incorporation, with dramatic enhancement in absorption intensity and spectral profile changes. Pure $CuFe_2O_4$ exhibits a broad absorption band around 460 nm, characteristic of *d-d* transitions in Cu^{2+} and Fe^{3+} ions within the spinel structure and charge transfer transitions between metal ions and oxygen. Upon silver doping, there is a progressive increase in overall absorption intensity and the emergence of additional absorption features, with the 5% Ag-doped sample showing peaks at 205 nm, 270 nm and 370 nm, while higher doping concentrations (10% and 20%) display intense absorption peaks around 270 nm and 259 nm, respectively. The intense absorption in the UV region (200-300 nm) can be attributed to ligand-to-metal charge transfer (LMCT) transitions involving silver ions and possible surface plasmon resonance effects from silver nanoparticles or clusters formed during synthesis. The dramatic increase in absorption intensity with increasing silver content, particularly evident in the 20% Ag-doped sample which shows the highest absorbance values, suggests enhanced light harvesting capability and potential photocatalytic applications. The red-shift and broadening of absorption bands indicate modification of the electronic band structure, reduced band gap energy and improved visible light absorption, making these materials promising candidates for solar energy conversion and photocatalytic degradation applications [40,42].

TABLE-2
FULL WIDTH HALF MAXIMUM (FWHM), CRYSTALLITE SIZE (D, nm) DATA OF $Ag_xCu_{1-x}Fe_2O_4$ (x = 0.05, 0.1, 0.2) NANOCOMPOSITES

2θ	θ (º)	Radian (θ)	FWHM degree (θ)	FWHM radian (θ)	Cos θ	D = 0.9λ/βCosθ	D (nm)
(a) $CuFe_2O_4$							
18.214	9.107	0.159	0.44791	0.008	0.987	179.74	17.97
29.899	14.949	0.261	0.45514	0.008	0.966	180.77	18.08
35.839	17.919	0.313	0.57368	0.010	0.952	145.62	14.56
37.074	18.537	0.323	0.67087	0.012	0.948	124.97	12.50
43.946	21.973	0.383	0.73111	0.013	0.927	117.24	11.72
53.926	26.963	0.470	0.38789	0.007	0.891	229.90	22.99
58.032	29.016	0.506	0.59421	0.010	0.875	152.96	15.30
63.827	31.914	0.557	1.00737	0.018	0.849	92.950	9.29
74.623	37.312	0.651	0.60665	0.011	0.796	164.71	16.47
							15.43
(b) 5%Ag-$CuFe_2O_4$							
18.35	9.17511	0.160	0.30534	0.005	0.987	263.715	26.371
30.059	15.0297	0.262	0.89348	0.016	0.966	92.119	9.212
35.958	17.9791	0.314	0.44813	0.008	0.951	186.487	18.649
37.121	18.5604	0.324	0.44247	0.008	0.948	189.505	18.951
43.913	21.9565	0.383	0.85149	0.015	0.928	100.651	10.065
58.018	29.0088	0.506	0.54978	0.010	0.875	165.310	16.531
63.839	31.9197	0.557	1.03432	0.018	0.849	90.532	9.053
74.929	37.4645	0.654	0.64097	0.011	0.794	156.211	15.621
							15.557
(c) 10%Ag-$CuFe_2O_4$							
18.286	9.14308	0.159	0.38555	0.007	0.987	208.833	20.883
30.057	15.0286	0.262	0.97887	0.017	0.966	84.082	8.408
34.905	17.4524	0.304	1.28346	0.022	0.954	64.922	6.492
37.107	18.5537	0.324	0.41993	0.007	0.948	199.669	19.967
43.919	21.9595	0.383	0.43122	0.008	0.928	198.751	19.875
57.994	28.9969	0.506	0.56435	0.010	0.875	161.023	16.102
63.837	31.9187	0.557	1.14665	0.020	0.849	81.662	8.166
74.689	37.3444	0.651	0.31201	0.005	0.795	320.394	32.039
							16.492
(d) 20%Ag-$CuFe_2O_4$							
18.224	9.11195	0.159	0.34563	0.006	0.987	232.932	23.293
30.01	15.0049	0.262	0.79170	0.014	0.966	103.949	10.395
35.505	17.7523	0.310	1.44779	0.025	0.952	57.649	5.765
38.082	19.0410	0.332	0.27516	0.005	0.945	305.603	30.560
44.041	22.0204	0.384	1.00269	0.017	0.927	85.512	8.551
57.836	28.9182	0.504	0.70496	0.012	0.875	128.808	12.881
64.387	32.1936	0.562	0.26040	0.005	0.846	360.672	36.067
77.393	38.6963	0.675	0.43686	0.008	0.781	233.085	23.308
							18.853

SEM studies: The SEM micrographs in Fig. 6a-d reveal distinct morphological variations in $Ag_xCu_{1-x}Fe_2O_4$ nanocomposites as silver concentration increases. The pristine $CuFe_2O_4$ exhibits agglomerated spherical particles with sizes ranging from 50-200 nm, forming clustered microstructures. Upon 5% silver incorporation, the morphology becomes more uniform with reduced agglomeration, indicating improved particle dispersion. The 10% silver-doped sample displays well-defined crystalline facets with particle sizes between 100-500 nm, suggesting enhanced crystallinity. At 20% Ag content, larger polyhedral particles emerge with distinct grain boundaries, reaching sizes up to 1 μm. This progressive morphological evolution demonstrates that silver doping significantly influences crystal growth kinetics and surface energy. The transition from spherical agglomerates to well-defined polyhedral structures indicates improved crystallographic ordering. The observed size increase with higher silver content suggests that Ag^+ ions act as structure-directing agents, promoting preferential crystal plane development and reducing surface defects in the spinel lattice [43,44].

Elemental analysis: The compositional analysis of Ag doped $CuFe_2O_4$ nanomaterials demonstrates consistent elemental distribution patterns as shown in Fig. 7a-d, which correspond to increasing the dopant concentrations. Silver incorporation escalates systematically from 5.03 wt.% to 18.32 wt.%, confirming effective integration within the crystalline framework. Simultaneously, oxygen composition decreases substantially from 84.49 wt.% (undoped material) to 72.42 wt.% (maximum silver loading), signifying considerable structural rearrangements throughout the doping process. Such compositional shifts indicate oxygen defect generation, potentially establishing the beneficial catalytic sites that accelerate photo-

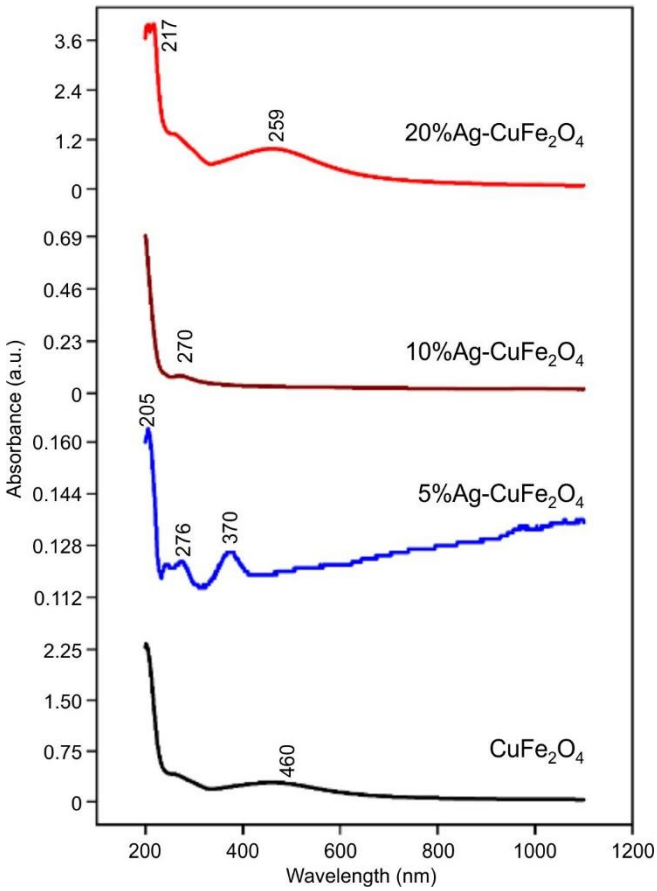

Fig. 5. UV-Vis spectra of microwave assisted synthesized $Ag_xCu_{1-x}Fe_2O_4$ (x = 0.05, 0.1, 0.2) nanocomposites

redox processes. Iron distribution undergoes dramatic alterations, declining from 12.54 wt.% in the parent compound to 4.30 wt.% at peak doping levels, whereas copper percentages maintain comparative stability across the 2.98-4.95 wt.% range as depicted in inset Fig. 7. This selective iron displacement indicates that silver cations preferentially occupy Fe^{3+} positions within the inverse spinel architecture, presumably governed by comparable ionic dimensions. The atomic fraction analysis validates this doping pattern, revealing diminished iron contribution alongside enhanced silver presence. Such elemental redistribution fundamentally modifies the electrical characteristics of the nanocomposite, establishing the interfacial boundaries that promote efficient electron-hole pair separation and boost photodegradation capabilities [45,46].

HR-TEM studies: The HRTEM analysis of biosynthesized $Ag_{0.1}Cu_{0.9}Fe_2O_4$ reveals well-crystallised nanoparticles with distinct morphological characteristics across different magnifications. At lower magnification, the particles exhibit spherical to quasi-spherical morphology with sizes ranging from 20-50 nm, demonstrating good dispersion with the minimal agglomeration. Higher magnification images clearly show lattice fringes, confirming the crystalline nature of the synthesised material. As seen in Fig. 8, the SAED pattern displays bright, well-defined spots arranged in concentric rings, characteristic of polycrystalline cubic spinel structure. The SAED patterns show distinct diffraction rings corresponding to (220), (311), (400), (511) and (440) planes, becoming more defined with increasing silver content, indicating improved crystallinity. The sharp diffraction spots indicate high crystallinity and absence of amorphous phases. The observed *d*-spacing values correspond to the major crystallographic planes of the spinel ferrite structure, consistent with XRD findings. Silver incorporation at 10% concentration maintains the structural integrity while enhancing crystalline quality. The uniform contrast distribution in HRTEM images suggests homogeneous silver distribution throughout the copper ferrite matrix, indicating the successful solid solution formation rather than phase segregation [47].

VSM studies: The magnetic characterization through vibrating sample magnetometry in Fig. 9a-d reveals the distinctive ferrimagnetic behaviour across all the synthesised compositions, with significant variations in the saturation magnetization values. Pure $CuFe_2O_4$ exhibits characteristic S-shaped hysteresis with saturation magnetization approaching 30 emu/g, confirming its inverse spinel structure. Silver incorporation progressively alters magnetic properties, where 5% Ag-doped samples demonstrate enhanced magnetization reaching approximately 250 emu/g, indicating favourable magnetic coupling between silver and iron cations within the crystalline framework. Interestingly, 10% silver doping maintains similar magnetic intensity while showing slightly modified coercivity patterns, suggesting structural stability despite increased dopant concentration. However, 20% Ag-$CuFe_2O_4$ displays reduced saturation magnetization around 85 emu/g, attributed to magnetic dilution effects where non-magnetic silver atoms disrupt magnetic exchange interactions between Fe^{3+} and Cu^{2+} ions [48]. The narrow hysteresis loops observed across all samples indicate soft magnetic characteristics with relatively low coercive fields, beneficial for potential applications requiring rapid magnetic response. These magnetic variations correlate directly with compositional changes, where the optimum Ag doping (5-10%) enhances the magnetic properties through improved crystallinity and reduced structural defects, while excessive doping (20%) leads to magnetic weakening due to disrupted spin arrangements and decreased magnetic moment per unit mass [49,50].

Antibacterial assays

Disk diffusion method: The $CuFe_2O_4$ nanoparticles had a weak antibacterial response, which shows that the ferrite matrix by itself has little bioactivity. However, upon Ag incorporation significantly improved inhibition behaviour with Ag-doped samples showing broader and stronger activity across bacterial and fungal strains (Table-3). This enhancement can be linked to silver-induced surface modification and defect generation within the spinel lattice, which likely promoted improved charge transfer and reactive species formation at the nanoparticle microbe interface [32,33]. Consequently, Ag doping effectively transformed $CuFe_2O_4$ into a more active multifunctional antimicrobial material.

Evaluation of DPPH free radical scavenging activity: The DPPH radical scavenging assay results demonstrate a marked enhancement in antioxidant properties upon silver doping into the copper ferrite matrix. The absorbance measurements (Table-4) reveal a systematic decrease with increasing sample concentration across all formulations, indicating effec-

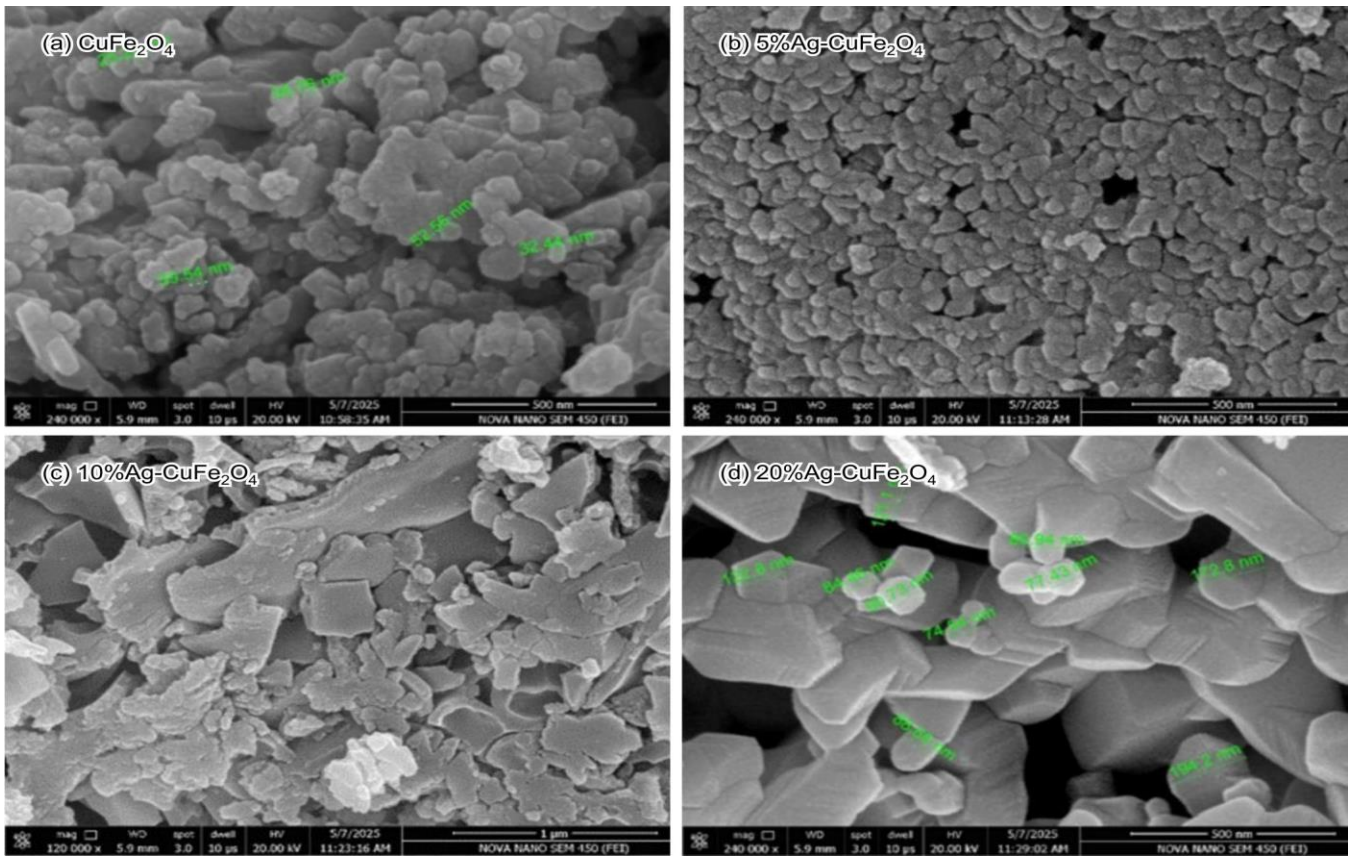

Fig. 6. SEM images of microwave assisted synthesized $Ag_xCu_{1-x}Fe_2O_4$ with silver doping levels of (a) 0%, (b) 5%, (c) 10% and (d) 20%

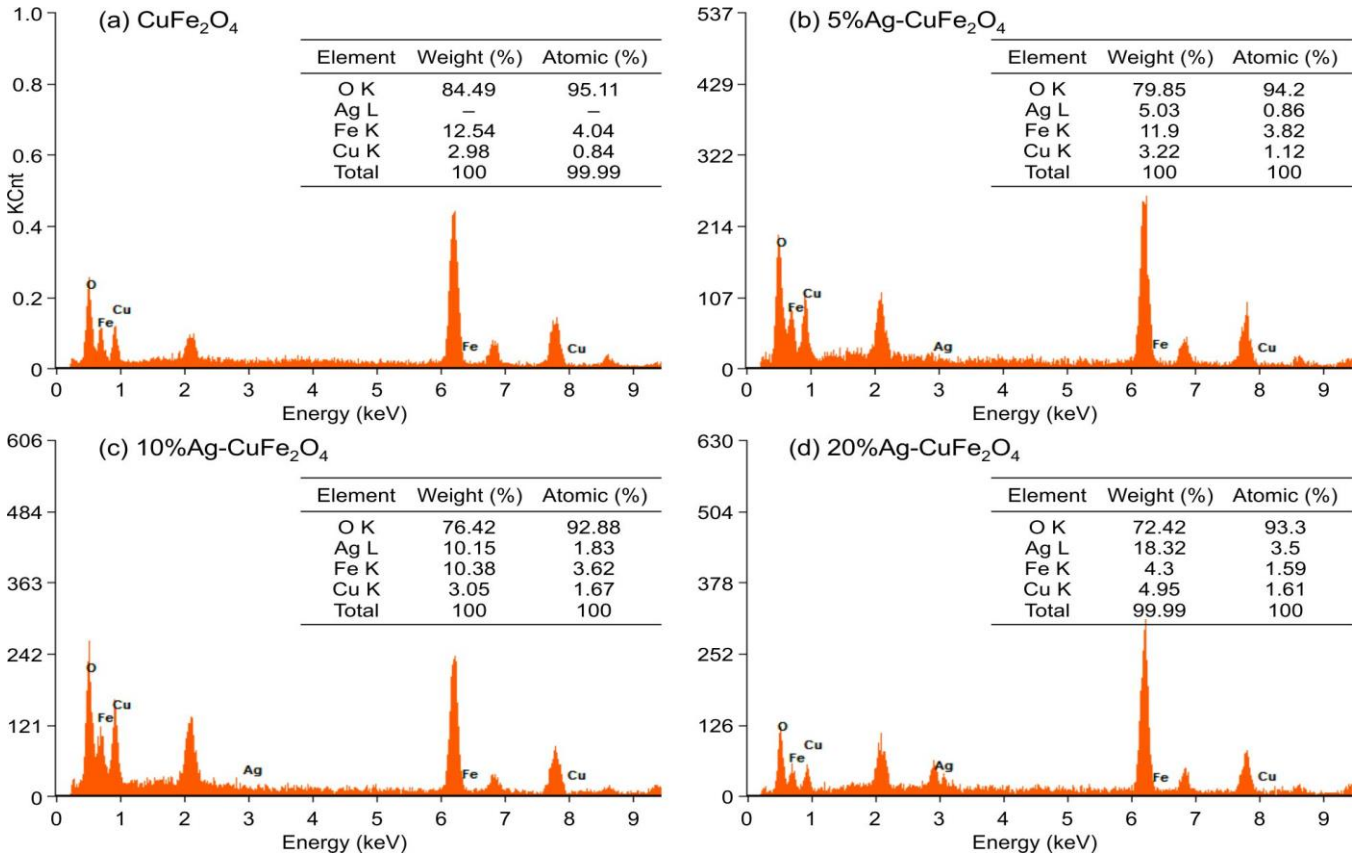

Fig. 7. EDAX spectra of microwave assisted synthesized $Ag_xCu_{1-x}Fe_2O_4$ (x = 0.05, 0.1, 0.2) nanocomposites

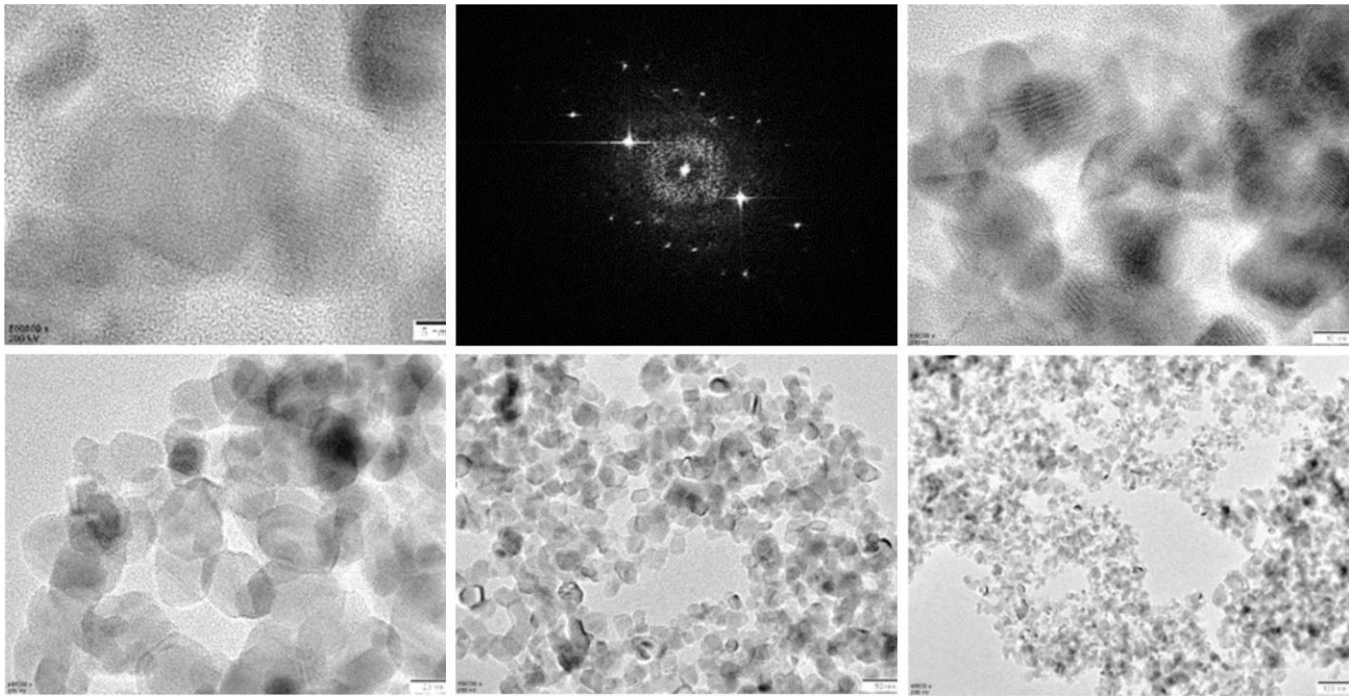

Fig. 8. HRTEM micrographs and SAED pattern of microwave assisted synthesized $Ag_{0.1}Cu_{0.9}Fe_2O_4$ nanocomposite

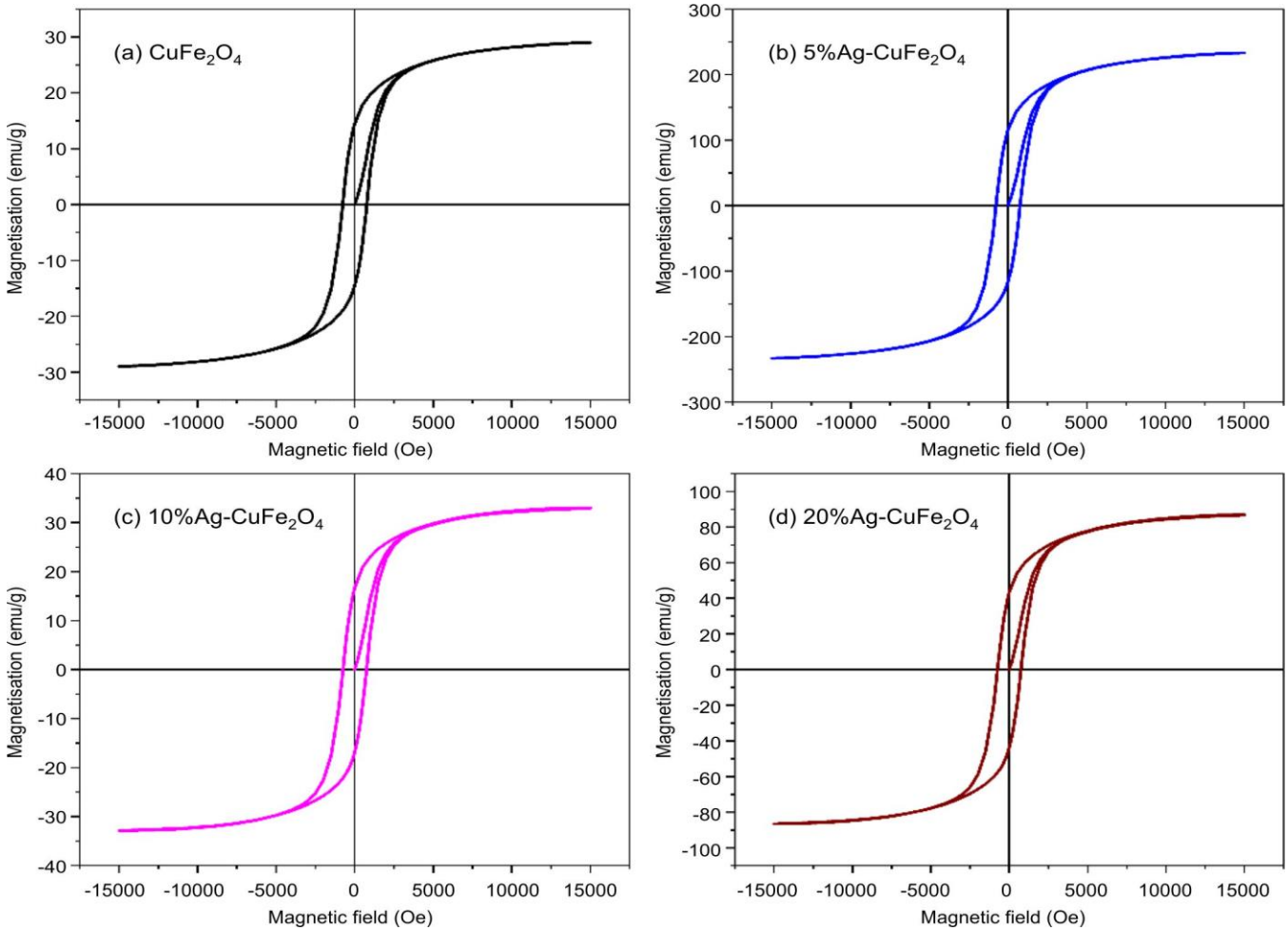

Fig. 9. Vibrating sample magnetometry (VSM) hysteresis loops of Ag-doped $CuFe_2O_4$ nanocomposites: (a) pristine $CuFe_2O_4$, (b) 5% Ag-$CuFe_2O_4$, (c) 10% Ag-$CuFe_2O_4$ and (d) 20% Ag-$CuFe_2O_4$

TABLE-3
ANTIMICROBIAL ACTIVITY DARA OF $CuFe_2O_4$ AND Ag-DOPED $CuFe_2O_4$ NANOCOMPOSITES

Samples	Sample code	Conc. (mcg/mL)	Inhibition zone (mm)					
			Antibacterial activity				Antifungal activity	
			Gram-positive		Gram-negative			
			Bacillus subtilis	*Staphylococcus aureus*	*Salmonella Typhimurium*	*Klebsiella pneumonia*	*Candida albicans*	*Aspergillus niger*
Standard (streptomycin)		10 µg/disc	18	20	22	16	22	22
$CuFe_2O_4$	CF01	20	12	0	18	0	0	11
$Ag_{0.05}Cu_{0.95}Fe_2O_4$	ACF01	20	9	14	16	11	19	16
$Ag_{0.1}Cu_{0.9}Fe_2O_4$	ACF02	20	10	12	15	14	16	18
$Ag_{0.2}Cu_{0.8}Fe_2O_4$	ACF03	20	8	16	12	15	15	19

TABLE-4
ABSORBANCE VALUES OF $CuFe_2O_4$ AND Ag-DOPED $CuFe_2O_4$ NANOCOMPOSITES AT DIFFERENT CONCENTRATIONS

Concentration (mg)	$CuFe_2O_4$	$Ag_{0.05}Cu_{0.95}Fe_2O_4$	$Ag_{0.1}Cu_{0.9}Fe_2O_4$	$Ag_{0.2}Cu_{0.8}Fe_2O_4$
Blank	0.972	0.972	0.972	0.972
50	0.758	0.745	0.738	0.722
100	0.732	0.720	0.712	0.690
150	0.708	0.658	0.632	0.625
200	0.642	0.628	0.612	0.584
250	0.565	0.528	0.513	0.434

tive radical neutralization. The Ag-doped variants exhibited lower absorbance values compared to pristine $CuFe_2O_4$, with $Ag_{0.2}Cu_{0.8}Fe_2O_4$ showing the most pronounced reduction at all tested concentrations. The calculated radical scavenging activity percentages (Table-5) substantiate this trend, where the highest silver-doped sample ($Ag_{0.2}Cu_{0.8}Fe_2O_4$) achieved 55.35% RSA at 250 mg concentration, significantly surpassing 41.87% observed for undoped $CuFe_2O_4$ as shown in Fig. 10. This progressive improvement correlates with the increasing silver content, suggesting that silver dopants introduce additional electron-donating sites that facilitate DPPH radical neutralization. The enhanced performance can be attributed to the synergistic interaction between silver nanoparticles and the ferrite host, creating a more efficient electron transfer mechanism.

The IC_{50} analysis (Table-6) provides contradictory data that requires careful interpretation. While lower IC_{50} values typically indicate superior antioxidant activity, the presented values show inconsistent patterns that may reflect calculation errors or methodological limitations as seen in Fig. 11. Future investigations should focus on standardizing the IC_{50} determination protocol and validating these measurements through complementary antioxidant assays such as ABTS or FRAP methods to establish comprehensive antioxidant profiles. The concentration-dependent behaviour observed across all the samples follows typical antioxidant kinetics, where higher

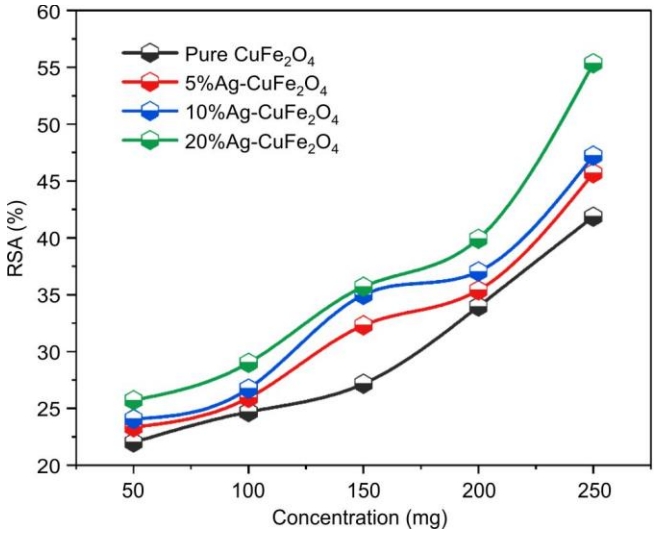

Fig. 10. DPPH radical scavenging activity (% RSA) profiles of $CuFe_2O_4$ and Ag-doped $CuFe_2O_4$ nanocomposites

material concentrations provide greater availability of active sites for radical scavenging. The silver doping effect becomes increasingly pronounced at higher concentrations, indicating that the enhanced antioxidant mechanism is dose-dependent and potentially governed by surface-mediated interactions between the nanoparticles and DPPH radicals [51,52].

TABLE-5
RADICAL SCAVENGING ACTIVITY (%RSA) $CuFe_2O_4$ AND Ag-DOPED $CuFe_2O_4$ NANOCOMPOSITES DATA AT VARIOUS CONCENTRATIONS

Concentration (mg)	$CuFe_2O_4$	$Ag_{0.05}Cu_{0.95}Fe_2O_4$	$Ag_{0.1}Cu_{0.9}Fe_2O_4$	$Ag_{0.2}Cu_{0.8}Fe_2O_4$
50	22.01646091	23.35390947	24.07407407	25.72016461
100	24.69135802	25.92592593	26.74897119	29.01234568
150	27.16049383	32.30452675	34.97942387	35.69958848
200	33.95061728	35.39094650	37.03703704	39.91769547
250	41.87242798	45.67901235	47.22222222	55.34979424

TABLE-6
IC_{50} VALUES OF $CuFe_2O_4$ AND Ag-DOPED $CuFe_2O_4$ NANOCOMPOSITES

Concentration (mg)	$CuFe_2O_4$	$Ag_{0.05}Cu_{0.95}Fe_2O_4$	$Ag_{0.1}Cu_{0.9}Fe_2O_4$	$Ag_{0.2}Cu_{0.8}Fe_2O_4$
50	201.8833536	38.57535754	164.7826087	133.8693467
100	505.6500608	176.0891089	429.8939555	343.2495812
150	809.4167679	313.6028603	695.0053022	552.6298157
200	1113.183475	451.1166117	960.1166490	762.0100503
250	1416.950182	726.1441144	1225.227996	971.3902848

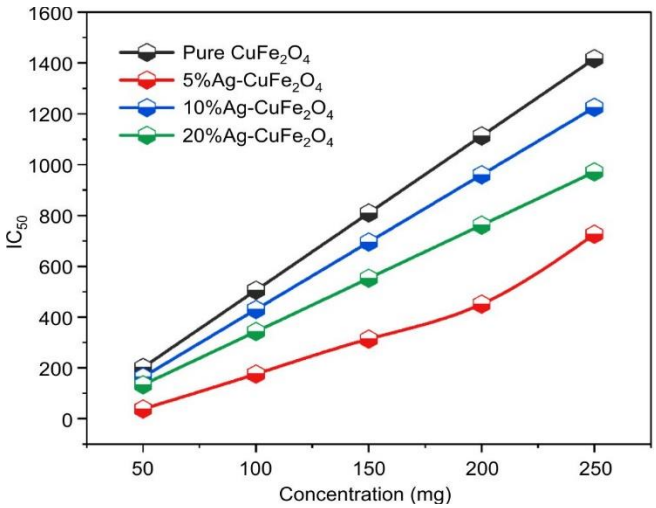

Fig. 11. IC_{50} profiles of $CuFe_2O_4$ and Ag-doped $CuFe_2O_4$ nanocomposites

Conclusion

The microwave-assisted biosynthesis of Ag-doped $CuFe_2O_4$ nanoparticles using *Asteracantha longifolia* leaf extract, offers an environmentally benign method for the development of ferrite materials, has been successfully achieved. Structural characterization confirmed the formation of pure cubic spinel phases with silver effectively integrated into the ferrite lattice without generating unwanted secondary phases. The changes in the lattice parameters (8.294 to 8.165 Å) and crystallite dimensions (15.43 to 18.85 nm) confirmed that the silver incorporation influences the fundamental material characteristics. Thermal analysis revealed stability up to 600 ºC, while optical studies showed enhanced UV-visible absorption capabilities. The biological evaluation yielded particularly promising results, with silver-doped samples displaying superior antimicrobial efficacy against both Gram-positive and Gram-negative bacterial strains, achieving inhibition zones of 8-19 mm. These findings confirmed the materials as excellent candidates for biomedical applications. The antioxidant assessment through DPPH radical scavenging assays revealed concentration-dependent activity enhancement with silver doping. The $Ag_{0.2}Cu_{0.8}Fe_2O_4$ composition achieved 55.35% radical scavenging activity at 250 mg concentration, substantially exceeding the 41.87% recorded for undoped copper ferrite.

CONFLICT OF INTEREST

The authors declare that there is no conflict of interests regarding the publication of this article.

DECLARATION OF AI-ASSISTED TECHNOLOGIES

During the preparation of this manuscript, the authors used an AI-assisted tool(s) to improve the language. The authors reviewed and edited the content and take full responsibility for the published work.

REFERENCES

1. T. Dippong, E.A. Levei and O. Cadar, *Nanomaterials*, **11**, 1560 (2021); https://doi.org/10.3390/nano11061560
2. M.M. Rashad, R.M. Mohamed, M. A. Ibrahim, L.F.M. Ismail and E.A. Abdel-Aal, *Adv. Powder Technol.*, **23**, 315 (2012); https://doi.org/10.1016/j.apt.2011.04.005
3. A. Soufi, H. Hajjaoui, R. Elmoubarki, M. Abdennouri, S. Qourzal and N. Barka, *Appl. Surf. Sci. Adv.*, **6**, 100145 (2021); https://doi.org/10.1016/j.apsadv.2021.100145
4. A.E. Danks, S.R. Hall and Z. Schnepp, *Mater. Horiz.*, **3**, 91 (2016); https://doi.org/10.1039/C5MH00260E
5. B. Niu, F. Zhang, H. Ping, N. Li, J. Zhou, L. Lei, J. Xie, J. Zhang, W. Wang and Z. Fu, *Sci. Rep.*, **7**, 3421 (2017); https://doi.org/10.1038/s41598-017-03644-6
6. K.B. Joshi, M.B. Nariya and B.J. Patgiri, *Int. J. Pharm. Pharmceut. Sci.*, **14**, 60 (2022); https://doi.org/10.22159/ijpps.2022v14i11.46148
7. A.K. Dash, G.K. Dutta, G. Sahoo, S.K. Mishra, K.K. Sardar and P.C. Bisoi, *J. Med. Plants Res.*, **6**, 3786 (2012).
8. S.R. Saple, S.E. Raval and V.V. Vaidya, Asian J. Pharm. Res. Health Care, **13**, 197 (2021); https://doi.org/10.18311/ajprhc/2021/27448
9. N. Phuyal, Ph.D. Thesis, The Chemical Characteristics and Antibacterial Activity of Green Tea (*Camellia sinensis*), Stinging Nettle (*Urtica diocia*) Leaves and the Blend, Department of Microbiology, Central Campus of Technology, Tribhuvan University, Dharan, Nepal (2021).
10. T. Misra, R. Singh, H. Pandey, B. Singh and R. Pandey, *Fitoterapia*, **72**, 194 (2001); https://doi.org/10.1016/S0367-326X(00)00269-0
11. D. Veerakumar and M. Muthulingam, *J. Pharm. Res. Int.*, **33**, 80 (2021); https://doi.org/10.9734/jpri/2021/v33i19B31340
12. O.Q. Adiamo, A.D.T. Phan, S. Akter, D. Sivakumar, P. Cunningham, F. Seke and Y. Sultanbawa, *Int. J. Food Sci. Technol.*, **59**, 573 (2024); https://doi.org/10.1111/ijfs.16572
13. S. Rao, *J. Cell Tissue Res.*, **13**, 3877 (2013).
14. A.K. Shukla, R.K. Malviya and J.N. Mishra, *Int. J. Health Sci.*, **6S1**, 14361 (2022); https://doi.org/10.53730/ijhs.v6nS1.8682
15. N.S. Chauhan and V.K. Dixit, *Rev. Bras. Farmacogn.*, **20**, 812 (2010); https://doi.org/10.1590/S0102-695X2010005000022
16. Z. Sun, L. Liu, D. Jia and W. Pan, *Sens. Actuators B Chem.*, **125**, 144 (2007); https://doi.org/10.1016/j.snb.2007.01.050
17. S. Anandan, T. Selvamani, G.G. Prasad, A. M. Asiri and J. J. Wu, *J. Magn. Magn. Mater.*, **432**, 437 (2017); https://doi.org/10.1016/j.jmmm.2017.02.026
18. D.V. Nair, N.B. Shridhar and K. Jayakumar, *Int. J. Nutr. Pharmacol. Neurol. Dis.*, **5**, 28 (2015); https://doi.org/10.4103/2231-0738.150072
19. N. Gammatantrawet, C.T. Nguyễn, C. Susawaengsup, A.N.M. Ramli, K. Tongkoom, T. Chatsungnoen, R. Dangtungee and P. Bhuyar, *Mol. Biotechnol.*, **67**, 885 (2025); https://doi.org/10.1007/s12033-024-01122-9

20. N. Chaudhary, Z. Roy, R. Bansal and L. Siddiqui, *Curr. Pharm. Biotechnol.*, **24**, 1265 (2023); https://doi.org/10.2174/1389201024666221121160822
21. K.N. Sunil Kumar, K.G. Divya, R. Mattummal, P. Sathiyarajeswaran, B. Erni and K. Kanakavalli, *Indian J. Pharm. Educ. Res.*, **55**, 36 (2021); https://doi.org/10.5530/ijper.55.1.7
22. S. Dubey, T. Virmani, S.K. Yadav, A. Sharma, G. Kumar and A. Alhalmi, *J. Nanomater.*, **2024**, 9914079 (2024); https://doi.org/10.1155/2024/9914079
23. A.M. Mohamed, *Academia Eng.*, **2024**, 1 (2024); https://doi.org/10.20935/AcadEng7302
24. S. Nayak, P. Ghugare and B. Vaidhun, *Indian J. Pharm. Educ. Res*, **55(2s)**, s510 (2021); https://doi.org/10.5530/ijper.55.2s.122
25. B. Uma, K.S. Anantharaju, B. Surendra, K. Gurushantha, S.S. More, S. Meena, B. Hemavathi and H.A. Murthy, *ACS Omega*, **8**, 9947 (2023); https://doi.org/10.1021/acsomega.2c07124
26. H. Jiao, G. Jiao and J. Wang, *Synth. React. Inorg. Met.-Org. Nano-Met. Chem.*, **43**, 131 (2013); https://doi.org/10.1080/15533174.2012.680090
27. N. El Messaoudi, Z. Ciğeroğlu, Z.M. Şenol, E.S. Kazan-Kaya, Y. Fernine, S. Gubernat and Z. Lopicic, *Biomass Convers. Biorefin.*, **15**, 99 (2025); https://doi.org/10.1007/s13399-023-05264-9
28. S.A. Jasim, I. Patra, M.J.C. Opulencia, K. Hachem, R.M.R. Parra, M.J. Ansari, A.T. Jalil, M.E. Al-Gazally, M. Naderifar, M. Khatami and R. Akhavan-Sigari, *Nanotechnol. Rev.*, **11**, 2483 (2022); https://doi.org/10.1515/ntrev-2022-0143
29. R. Skov, R. Smyth, A. Larsen, A. Bolmstrom, A. Karlsson, K. Mills, N. Frimodt-Moller and G. Kahlmeter, *J. Clin. Microbiol.*, **44**, 4395 (2006); https://doi.org/10.1128/JCM.01411-06
30. H. Fujikawa and M. Matsushita, *J. Phys. Soc. Jpn.*, **58**, 3875 (1989); https://doi.org/10.1143/JPSJ.58.3875
31. S.A. Waksman, *Science*, **118**, 259 (1953); https://doi.org/10.1126/science.118.3062.259
32. S. Kalia, V. Dhiman and N. Prasad, *Mater. Chem. Phys.*, **334**, 130417 (2025); https://doi.org/10.1016/j.matchemphys.2025.130417
33. K. Atacan, M. Özacar and M. Özacar, *Int. J. Biol. Macromol.*, **109**, 720 (2018); https://doi.org/10.1016/j.ijbiomac.2017.12.066
34. İ. Gulcin and S.H. Alwasel, *Processes*, **11**, 2248 (2023); https://doi.org/10.3390/pr11082248
35. S.B. Kedare and R. Singh, *J. Food Sci. Technol.*, **48**, 412 (2011); https://doi.org/10.1007/s13197-011-0251-1
36. M.C. Foti, *J. Agric. Food Chem.*, **63**, 8765 (2015); https://doi.org/10.1021/acs.jafc.5b03839
37. M. Hashemi, S. Abolghasemi, F. Rahimi, S. Rajabi and A. Nasiri, *J. Environ. Manage.*, **373**, 123978 (2025); https://doi.org/10.1016/j.jenvman.2024.123978
38. S. Rajabi, Z. Derakhshan, S. Maleky, A. Nasiri, B. Ahmadi, M. Feilizadeh, A. Mohammadpour, M.R. Samaei and M. Hashemi, *Int. J. Biol. Macromol.*, **286**, 138375 (2025); https://doi.org/10.1016/j.ijbiomac.2024.138375
39. E.J. Abdelrazek, A.A. Gahlan, G.A. Gouda and A.S. Ahmed, *Sci. Rep.*, **15**, 4123 (2025); https://doi.org/10.1038/s41598-025-86209-2
40. M. Sangeetha, S. Ambika, D. Madhan and S. Vadivel, *J. Mater. Sci. Mater. Electron.*, **35**, 368 (2024); https://doi.org/10.1007/s10854-024-12076-8
41. M. Pourshaban-Mazandarani and A. Nasiri, *J. Polym. Environ.*, **32**, 5713 (2024); https://doi.org/10.1007/s10924-024-03340-3
42. Z. Zhu, X. Li, Q. Zhao, Y. Li, C. Sun and Y. Cao, *Mater. Res. Bull.*, **48**, 2927 (2013); https://doi.org/10.1016/j.materresbull.2013.04.042
43. F. Mohammed A. Alzahran, J. Arshad, M.S. Al-Buriahi, Z.A. Alrowaili and S. Munir, *J. Taibah Univ. Sci.*, **17**, 2209676 (2023); https://doi.org/10.1080/16583655.2023.2209676
44. B. Surendra, *J. Sci. Adv. Mater. Devices*, **3**, 44 (2018); https://doi.org/10.1016/j.jsamd.2018.01.005
45. N. Kahzad and A. Salehzadeh, *Biol. Trace Elem. Res.*, **198**, 359 (2020); https://doi.org/10.1007/s12011-020-02055-5
46. M. Giridhar, B. Manjunath, B. Surendra, K. Harish, S. Prashantha, T. Kiran, B. Uma and H.A. Murthy, *Sci. Rep.*, **13**, 17821 (2023); https://doi.org/10.1038/s41598-023-45029-y
47. S. Malvilayila, M. Fukateb, *Int. J. Environ. Sci.*, **11**, 660 (2025); https://doi.org/10.64252/g2eztw05
48. A.R. Chavan, S.B. Bhosale, S.B. Somvanshi, P.P. Khirade, *J. Sol-Gel Sci. Technol.*, **116**, 434 (2025); https://doi.org/10.1007/s10971-025-06730-8
49. A. Pawar, B. Patil, S. Bhongale, A. Salunkhe, S. Kumar and T. Shinde, *Indian J. Phys. Proc. Indian Assoc. Cultiv. Sci.*, **96**, 3161 (2022); https://doi.org/10.1007/s12648-021-02245-4
50. S.M. Rathod, A.R. Chavan, S.S. Jadhav, K.M. Batoo, M. Hadi and E.H. Raslan, *Chem. Phys. Lett.*, **765**, 138308 (2021); https://doi.org/10.1016/j.cplett.2020.138308
51. K.H. Musa, A. Abdullah and A. Al-Haiqi, *Food Chem.*, **194**, 705 (2016); https://doi.org/10.1016/j.foodchem.2015.08.038
52. N. Nenadis and M. Tsimidou, *J. Am. Oil Chem. Soc.*, **79**, 1191 (2002); https://doi.org/10.1007/s11746-002-0626-z